Angle-resolved photoemission extended fine structure of the Ni $3p$, Cu $3s$, and Cu $3p$ core levels of the respective clean (111) surfaces

W. R. A. Huff

Lawrence Berkeley National Laboratory, Berkeley, California 94720
and The University of California, Department of Chemistry, Berkeley, California 94720

Y. Chen

The Pennsylvania State University, Department of Chemistry and Physics, University Park, Pennsylvania 16802

S. A. Kellar and E. J. Moler

Lawrence Berkeley National Laboratory, Berkeley, California 94720
and The University of California, Department of Chemistry, Berkeley, California 94720

Z. Hussain

Lawrence Berkeley National Laboratory, Berkeley, California 94720

Z. Q. Huang

James Franck Institute, University of Chicago, Illinois 60637

Y. Zheng

Oplink, San Jose, California 95131

D. A. Shirley

The Pennsylvania State University, Department of Chemistry and Physics, University Park, Pennsylvania 16802

We report a non-s initial-state angle-resolved photoemission extended fine-structure (ARPEFS) study of clean surfaces for the purpose of further understanding the technique. The surface structure sensitivity of ARPEFS applied to clean surfaces and to arbitrary initial states is studied using normal photoemission data taken from the Ni $3p$ core levels of a Ni(111) single crystal and the Cu $3s$ and the Cu $3p$ core levels of a Cu(111) single crystal. The Fourier transforms of these clean surface data are dominated by backscattering. Unlike the s initial-state data, the p initial-state data show a peak in the Fourier transform corresponding to in-plane scattering from the six nearest neighbors to the emitter. Evidence was seen for single-scattering events from the same plane as the emitters and double-scattering events. Using a recently developed, multiple-scattering calculation program, ARPEFS data from clean surfaces and from p initial states can be modeled to high precision. Although there are many layers of emitters when measuring photoemission from a clean surface, test calculations show that the ARPEFS signal is dominated by photoemission from atoms in the first two crystal layers. Thus ARPEFS applied to clean surfaces is sensitive to surface reconstruction. The best-fit calculation for clean Ni(111) indicates an expansion of the first two layers. [S0163-1829(97)01527-0]

I. INTRODUCTION

Angle-resolved photoemission extended fine structure (ARPEFS) is a well-established technique for determining surface structures.[1–5] ARPEFS has been used to determine the structures of adsorbate systems as well as molecular adsorbates on conducting single-crystal surfaces. ARPEFS yields precise information about both the local structure around the adsorbates and the adsorbate-induced relaxation of the substrates.[6–12] These studies have shown that ARPEFS data and their Fourier transforms (FT's) can be described mainly in terms of backscattering events. The positions of all the strong peaks in ARPEFS FT's from adsorbates can be predicted from a trial structure with fairly good accuracy based on a single-scattering cluster model together with the

concept of a backscattering cone.

The purpose of this paper is to explore the applicability of ARPEFS to non-s initial-state photoemission from clean surfaces. The immediate goal is to observe and to understand the phenomenon in a simple, known system. The long-range goal is to develop a method for studying photoemission from arbitrary initial states as well as to determine the atomic structure of interfaces, for which ARPEFS seems ideally suited. In favorable cases, atomic relaxation and reconstruction could be studied as well. In such studies, the elemental and chemical specificity of ARPEFS and its sensitivity to atomic layers that are several layers below the surface would be advantageous.

If the photoelectron signals from surface and bulk atoms are resolvable in ARPEFS studies of clean surfaces, then the

data analysis may be based on multiple ARPEFS curves. For the more common case in which signals from different layers cannot be resolved, reconstruction or relaxation effects may still be modeled by fitting the single experimental ARPEFS curve. In the absence of a surface core-level shift, the ARPEFS curve may or may not be surface sensitive enough to yield a conclusion about a possible surface reconstruction.

Most of the previous ARPEFS studies have been based on photoemission data from atomic s core-level initial states, for which the dipole selection rules $\Delta l_i = \pm 1$ and $\Delta m_i = 0$ give a p_0-wave final state. Experience with ARPEFS data from non-s initial states and their FT's is very limited, however.[13–15] For non-s initial states ($l_i \neq 0$), partial waves with orbital quantum numbers $l_i + 1$ and $l_i - 1$ contribute to the photoemission intensity. There is a phase relationship between them that leads to interference between the partial waves. Note that the allowed m levels will be populated in the final state. Thus, with a p initial state, the photoemitted partial waves consist of $l_f = 0$ and $m_f = m_i = 0$ as well as $l_f = 2$ and $m_f = m_i = 0, \pm 1$. The partial-wave radial dipole matrix elements and the phase shifts are generally energy dependent. It is important to note that the *intensities* from the different m levels are summed, not the amplitudes.[16] The intensities are also summed over the different emitters e. Thus, for the given partial waves $\psi_{l_f, m}(\theta, \phi, k)$, the total intensity from an isolated atom $I_{\text{tot}}(\theta, \phi, k)$ is

$$I_{\text{tot}}(\theta, \phi, k) = \sum_e \sum_m \left| \sum_{l_f} (-i)^{l_f} R_{l_f}(k) e^{i\delta_{l_f}(k)} \right.$$
$$\left. \times \langle Y_{l_f, m} | Y_{1,0} | Y_{l_i, m} \rangle \psi_{l_f, m}(\theta, \phi, k) \right|^2 . \quad (1)$$

$\langle Y_{l_f, m} | Y_{1,0} | Y_{l_i, m} \rangle$ is the overlap integral between the initial and final spherical harmonic wave functions, which are functions of θ and ϕ. $R_{l_f}(k)$ are the partial-wave radial dipole matrix elements and $\delta_{l_f}(k)$ are the phase shifts. Despite these complications, there are a number of experimental situations for which ARPEFS from an arbitrary initial state may be the most suitable method of study.

Two different data sets are presented here. The first set is from the $3p$ core levels of a clean Ni(111) surface. Due to fitting complications caused by the satellites [Fig. 1(a)], a second ARPEFS data set was taken from the Cu $3s$ and the Cu $3p$ [Fig. 1(b)] core levels of a clean Cu(111) single crystal. These Cu $3s$ and Cu $3p$ data are used to study the non-s initial-state photoemission from a clean surface in a carefully controlled manner.

Section II discusses the experimental details. Sections III, IV, V, and VI discuss the data reduction, the Fourier analysis, the multiple-scattering analysis, and the error analysis, respectively. Section VII provides a discussion, which includes a comparison between the nickel data and an adsorbate system as well as some test calculations performed to better understand the scattering processes. Section VIII is a conclusion.

II. EXPERIMENT

The data were collected in an ultrahigh-vacuum chamber (with pressure ≤ 60 nPa) equipped with a rotatable, angle-
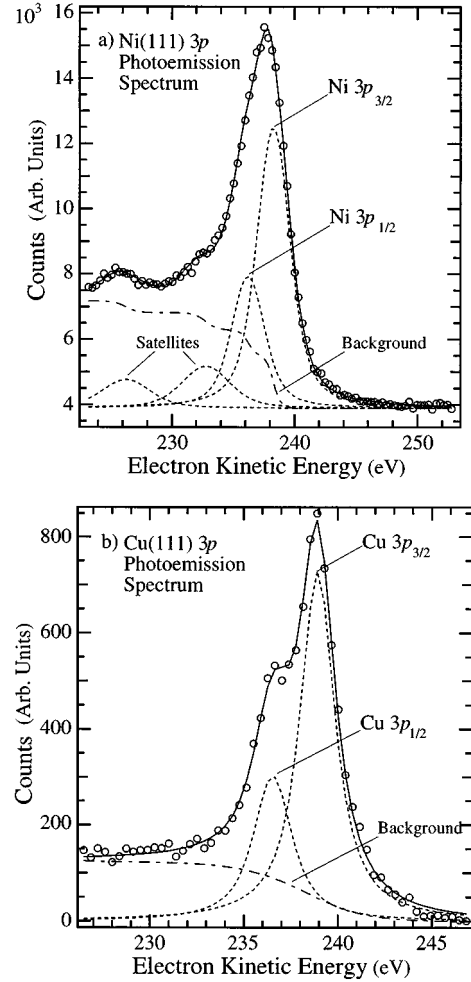

FIG. 1. Example photoemission spectrum showing (a) the Ni(111) $3p$ data and (b) the Cu $3p$ data as well as the Voigt functions and the step functions used to fit the data.

resolved, hemispherical electron energy analyzer[17] and standard ultrahigh-vacuum surface science instrumentation. The sample manipulator allows for either liquid-nitrogen or liquid-helium cooling. The crystals were cleaned by repetitive cycles of Ar$^+$ sputtering and subsequent annealing by e-beam heating to 700 °C. The sample cleanliness was monitored using synchrotron x-ray photoemission spectroscopy.

The Ni(111) experiment was performed at the National Synchrotron Light Source at Brookhaven National Laboratory on beamline U3-C. The crystal was cooled to $\lesssim 100$ K throughout the data collection; no contamination was detected before or after the Ni data collection, which lasted 9.5 h. The light was oriented 55° from the surface normal away from the crystal (011) plane. The photon polarization vector ε was thus oriented 35° from the surface normal and perpendicular to the crystal (011) plane (see illustration in Fig. 2). The analyzer was oriented 4° off normal from the Ni(111). The total experimental energy resolution was ~3.0 eV.

The Cu(111) experiments were performed using the Advanced Light Source at the E. O. Lawrence Berkeley National Laboratory on beamline 9.3.2.[18] The crystal was cooled to ~80 K throughout the data collection, which lasted 5 h for each ARPEFS curve. The photon polarization vector ε was oriented 10° from the surface normal (see illustration
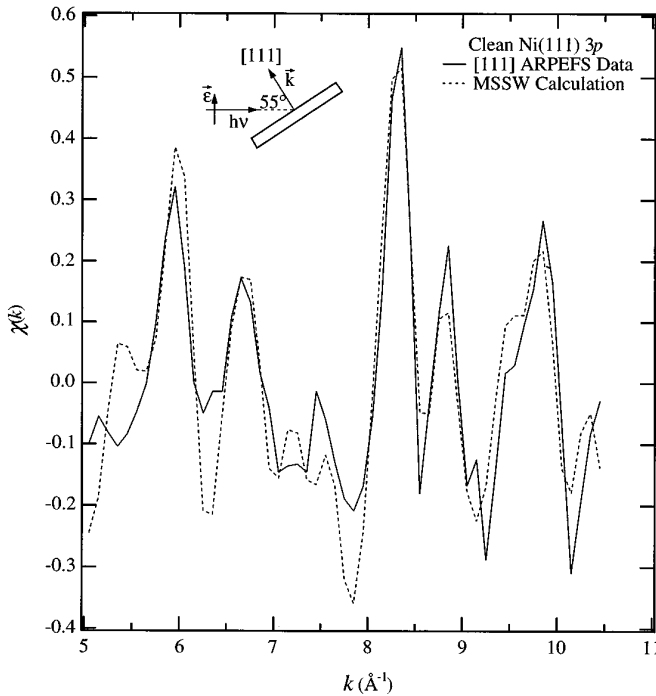
FIG. 2. Ni(111) $3p$ ARPEFS $\chi(k)$ data (solid line) and best fit (dashed line). A schematic of the experimental geometry is shown.

in Fig. 3). The analyzer was oriented 5° from the surface normal.

The raw ARPEFS data are a series of x-ray photoemission spectra, each with a different kinetic energy. The magnitude of the photoelectron wave vector ranged from 5.1 to 10.5 Å^{-1} for the nickel data and from 5.0 to 11.9 Å^{-1} for both copper data sets. All of the spectra were recorded in equal 0.1-Å^{-1} steps.
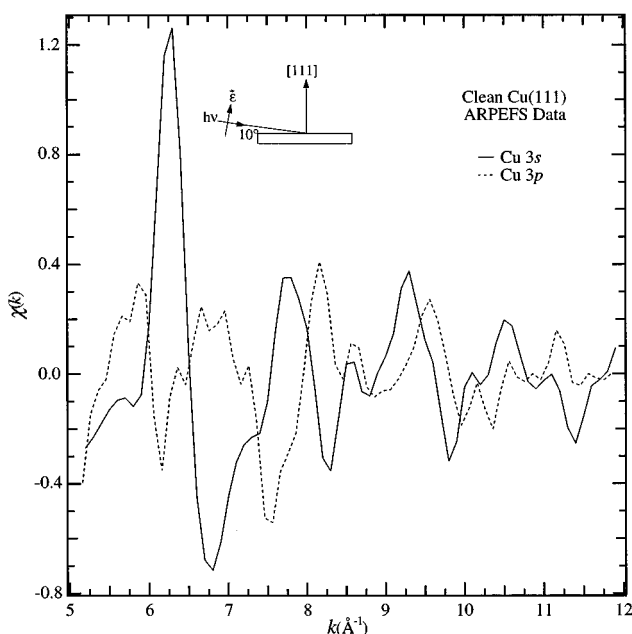

FIG. 3. Comparison of the Cu(111) $3s$ (solid line) and $3p$ (dashed line) ARPEFS $\chi(k)$ data. A schematic of the experimental geometry is shown.

III. DATA REDUCTION

Each peak was fit with a Voigt function added to a step function with a step height scaled to the respective peak intensity and a step width taken as the Gaussian width of the peak. This step function models the inelastic-scattering background of the photoemission spectrum. The total fit is the solid line through the data points in Figs. 1(a) and 1(b).

The purpose of fitting the spectra is to extract the most accurate area from the peaks, reducing the data to the $\chi(k)$ diffraction curve, which contains the structural information. $\chi(k)$ is defined by[19]

$$\chi(k) = \frac{I(k)}{I_0(k)} - 1, \qquad (2)$$

where $I(k)$ is the peak area plotted as a function of the peak position in k. $I_0(k)$ is a smooth, slowly varying function with an oscillation frequency much lower than $I(k)$; $I_0(k)$ stems from the contribution of the inelastic background and the atomic cross section. It is adequate to use a simple spline function to fit $I_0(k)$.[20]

Removing $I_0(k)$ results in a suppression of the FT the peaks $\lesssim 2$ Å. In photoemission from clean surfaces, many forward-scattering path-length differences from subsurface emitters will be $\lesssim 2$ Å. This forward-scattering signal is therefore removed during the data reduction along with the $I_0(k)$. The extracted experimental ARPEFS $\chi(k)$ curve is thus dominated by backscattering.

Figure 2 plots the Ni $3p$ experimental $\chi(k)$ curve (solid line), which represents the sum of the Ni $3p_{3/2}$ and Ni $3p_{1/2}$ areas shown in Fig. 1(a). The best-fit result from the multiple-scattering modeling calculations is also shown in Fig. 2 (dashed line) and will be discussed in Sec. V.

Figure 3 overlays the Cu $3s$ and the Cu $3p$ ARPEFS $\chi(k)$ curves. The experimental geometry is also shown. The data are plotted in this way to clearly illustrate that the ARPEFS data from an s atomic core level are $\sim 180°$ out of phase from ARPEFS data from a p atomic core level. This result is expected and has been studied previously.[13–15]

IV. FOURIER ANALYSIS

It is useful to study the autoregressive linear-prediction-based (ARLP) Fourier transform to transform from momentum space to real space.[2,5,6,21] In ARPEFS, the positions of the strong peaks in ARLP FT's from adsorbate/substrate systems can be predicted with fairly good accuracy using the single-scattering cluster model together with the concept of strong backscattering from atoms located within a cone around 180° from the emission direction. The effective solid angle of this backscattering cone is $\sim 30°-60°$; it is not unique, but is operationally defined simply by opening the angle until it can account for the observed FT peaks based on the crystal geometry. Signals from scattering atoms very close to the source atom may be observable, even if the scatterers lie outside the nominal backscattering cone.

The FT peaks correspond to path-length differences (PLD's) ΔR_j between the component of the photoelectron

wave that propagates directly to the detector and the components that are first scattered by the atomic potentials within this backscattering cone.[6] Thus the peak positions are approximately

$$\Delta R_j = r_j (1 - \cos\theta_j), \qquad (3)$$

where r_j is the bond length from the emitter to a given atom j and θ_j is the scattering angle (180° for exact backscattering). Note that the effect of the atomic scattering phase shift is ignored in this approximation. The scattering takes place inside the crystal and the ARPEFS data must be shifted from the measured $\chi(k_{\text{outside crystal}})$ to $\chi(k_{\text{inside crystal}})$ to account for the inner potential. In ARPEFS modeling calculations, the inner potential is treated as an adjustable parameter and is typically 5–15 eV. The inner potential is approximately the sum of the work function and the valence bandwidth.[22] Thus, before Fourier transformation, the ARPEFS data presented here were shifted by 10 eV to higher kinetic energy.

A. Ni(111)

The ARLP FT of the Ni $3p$ experimental ARPEFS data is plotted in Fig. 4(a). Also illustrated in Fig. 4 is a schematic of a [111] single crystal, assuming a bulk-terminated fcc surface, with a backscattering cone superimposed. The FT shows peaks due to scattering from atoms up to four layers below the emitting atoms. The depth sensitivity of ARPEFS has been described previously and was found to be enhanced by multiple-scattering effects.[5]

The atoms and corresponding peaks are labeled in Fig. 4. Using the bulk nickel nearest-neighbor spacing 2.49 Å, the expected peak positions can be calculated using simple geometry. These expected peak positions along with the experimental peak positions and their corresponding shifts are listed in Table I. Table I also lists an assignment of each peak to single-scattering (SS) or double-scattering (DS) events. Additionally, the number of atoms contributing to each peak is listed in Table I.

The origins of the peaks labeled 2–6 are straightforward. If a line is drawn from a surface emitter into the crystal and normal to the (111) plane, peaks 2, 3, and 6 occur due to single scattering from the three atoms closest to this line in layers 2, 3, and 5, respectively. Nickel has a fcc crystal structure and thus peak 4 is due to direct backscattering ($\theta_j = 180°$) from atom 4, which is in layer 4. Peak 5 is due to single scattering from atoms 5, which are the six nearest neighbors to atom 4.

Peaks 2′ and 3′ may be attributed to atoms more laterally distant from the line described above. Peak 2′ occurs due to single scattering from the three second-nearest neighbors to this line in layer 2. Similarly, peak 3′ occurs due to single scattering from the three second-nearest neighbors to this line in layer 3.

Double scattering may be detectable in the ARLP FT as evidenced by peaks 2*, 3*, 4*, and 5*. The first event for peak 2*, for example, is scattering by atoms 2. The second event is scattering by the six nearest neighbors of atoms 2. Given that there are three atoms 2, eighteen atoms are available for the second scattering event to give peak 2*. An analogous process holds for the 3* peak. Because there is only one atom 4 for each emitter in the fcc (*abcabc*) geom-
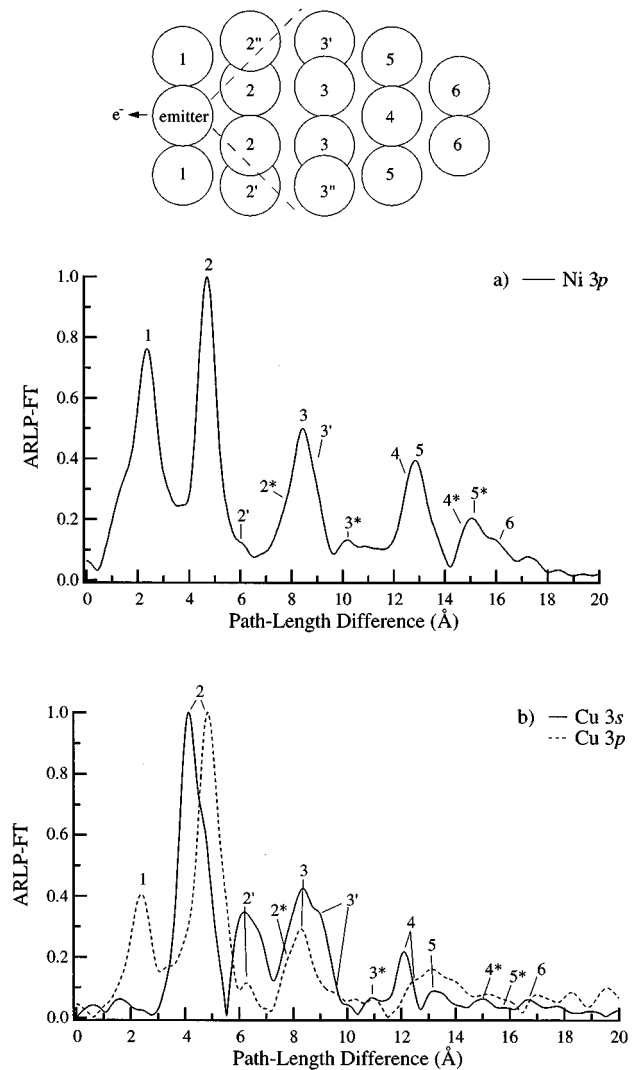

FIG. 4. ARLP-based FT of (a) the Ni $3p$ and (b) the Cu $3s$ (solid line) and Cu $3p$ (dashed line) ARPEFS data. A model of the lattice with the backscattering cone indicates the scattering atoms corresponding to the FT peaks.

etry, only six atoms are in position for the second scattering event to give peak 4*. However, there are six atoms 5 and thus thirty-six atoms for the second scattering event to give peak 5*.

These assignments due to double scattering are somewhat speculative. It is believed that peaks 4* and 5* have a higher relative amplitude as compared to 2* and 3* because waves scattering in the fourth layer can be forward focused by atoms in the surface layer. Also, the higher probability for the second scattering event of peak 5* due to the greater number of atomic potentials will increase its relative amplitude.

A different result is also noted in this ARLP FT. The peak labeled 1 is due to in-plane scattering of the photoemission wave from the six nearest neighbors to the emitter. In-plane scattering for normal emission has not been observed previously for s initial-state data or calculations. In s initial-state photoemission, the outgoing p_0 wave destructively interferes with itself for $\theta_j = 90°$ due to the negative parity of a p wave. In p initial-state photoemission, however, the photoemitted d and s waves, which are interfering with themselves

TABLE I. Scattering paths with the calculated PLD's for Ni(111) (based on 2.49-Å nearest-neighbor spacing) along with the experimental peak positions and the respective shifts. Layer 1 is defined as the same layer as the emitter. Refer to Fig. 4 for an illustration of the atomic positions. SS indicates single scattering and DS indicates double scattering.

Peak number	Geometric PLD (Å)	Peak position (Å)	Peak shift (Å)	Scattering process	No. of atoms
1	2.49	2.36	−0.13	SS	6
2	4.52	4.69	0.17	SS	3
2′	5.55	5.99	0.44	SS	3
2*	7.01	7.60	0.59	DS	3×6
3	8.37	8.45	0.08	SS	3
3′	9.04	9.07	0.03	SS	3
3*	10.86	10.18	−0.68	DS	3×6
4	12.18	12.51	0.33	SS	1
5	12.67	12.90	0.23	SS	6
4*	14.67	14.68	0.01	DS	1×6
5*	15.16	15.09	−0.07	DS	6×6
6	16.37	16.00	−0.37	SS	3

and with each other, have positive parity and do not cancel for normal emission, in-plane scattering. Thus the frequency component labeled peak 1 is a physical part of the $\chi(k)$ diffraction curve and the appropriate PLD peak is observed. A peak that would be labeled 1′ arising from in-plane scattering by the second-nearest neighbors would be seen at ~4.31 Å. If present, this weak feature is obscured by peak 2.

B. Cu(111)

Figure 4(b) plots the ARLP FT of the Cu 3s and the Cu 3p ARPEFS data. The interpretation of each FT peak is similar to the Ni FT discussion above. Cu(111) is also fcc and the bulk nearest-neighbor spacing is 2.56 Å.

The expected peak positions are listed in Table II along with the experimental peak positions and corresponding shifts for the Cu 3s and Cu 3p data FT's. Table II also lists

an assignment of each peak to SS or DS events. Additionally, the number of atomic scattering potentials contributing to each peak is listed in Table II.

From the single-scattering values listed in Table II, one can see that the structure can generally be determined to ±0.5 Å by simply analyzing the ARLP FT. Given this precision, some peaks seem to correlate with double-scattering PLD's. Again, these assignments due to double-scattering events are somewhat speculative. To be certain that these small features are not artifacts caused by the finite data range, one must study the FT in more detail than has been done to date. Additionally, one must better understand any slight shifting of the peaks resulting from mathematically extending the data range using the ARLP method.

An interesting feature of the Cu 3s FT as compared to the Cu 3p FT is the intensity differences between some of the peaks. If the ARPEFS data from these different initial states were identical but out of phase, then their respective peak

TABLE II. Scattering paths with the calculated PLD's for Cu(111) (based on 2.56-Å nearest-neighbor spacing) along with the experimental peak positions and the respective shifts. Refer to Fig. 4 for an illustration of the atomic positions.

Peak number	Geometric PLD (Å)	Cu 3s position (Å)	Cu 3s shift (Å)	Cu 3p position (Å)	Cu 3p shift (Å)	Scattering process	No. of atoms
1	2.56			2.39	0.17	SS	6
2	4.65	4.15	−0.50	4.85	+0.20	SS	3
2′	5.71	6.19	+0.48	6.26	+0.55	SS	3
2*	7.21	7.67	+0.46	7.58	+0.37	DS	3×6
3	8.61	8.36	−0.25	8.29	−0.32	SS	3
3′	9.30	8.91	−0.39	9.37	+0.07	SS	3
3*	11.17	10.91	−0.26	10.97	−0.20	DS	3×6
4	12.54	12.10	−0.44	12.46	−0.08	SS	1
5	13.04	13.20	+0.16	13.12	+0.08	SS	6
4*	15.10	14.96	−0.14	15.13	+0.03	DS	1×6
5*	15.60	15.77	+0.17	15.80	+0.20	DS	6×6
6	16.85	16.68	−0.17	16.99	+0.14	SS	3

positions and intensities would be identical. These data are more than simply out of phase. Peak 1 in the Cu $3p$ FT is not present in the Cu $3s$ FT. The origin of peak 1 is analogous to peak 1 in the Ni $3p$ FT.

V. MULTIPLE-SCATTERING ANALYSIS

Calculations were performed to model the ARPEFS $\chi(k)$ curves. Modeling calculations are very useful because, in addition to allowing a precise structure determination, a variety of test cases can be used to better understand the scattering processes. Using the single-scattering model of ARPEFS,[6,19] $\chi(k)$ is written as

$$\chi(k) = \sum_j A_j(k) \cos[k(R_j - R_j \cos\theta_j) + \phi(k)], \quad (4)$$

where $A_j(k)$ contains experimental geometry factors including the photon polarization direction and the electron emission direction as well as the scattering amplitude, angle integration, and thermal averaging. $\phi(k)$ is the atomic scattering phase shift.

At $\theta_j = 0°$, there is zero PLD between the direct and scattered photoelectron waves. For forward scattering through angles close to $0°$, the scattering amplitude is quite large, but many path-length differences are correspondingly small and do not show up in the FT's.

The multiple-scattering spherical-wave (MSSW) code developed by Barton et al.[6,19,20,23] has been proven to precisely model s initial-state core-level photoemission.[6-11] However, the ARPEFS data and FT's from a p initial state require both s and d partial waves to describe the photoemission signal. Kaduwela[24] developed a code based on the Rehr-Albers formalism,[25] which has been discussed and applied to photoelectron diffraction from arbitrary initial states by Friedman and Fadley.[26] Another code developed by Chen, Wu, and Shirley,[27] which is also based on the Rehr-Albers formalism,[25] was used for the calculations presented here. Due to the summing methods used in this code, it is significantly faster than the previous codes. Thus, fitting calculations can be performed for systems in which the photoemitters are in many layers and the core-level initial state has arbitrary angular momentum.

For the Ni $3p$ and the Cu $3p$ calculations, the radial dipole matrix elements $R_{l_i \pm 1}$ and phase shifts $\delta_{l_i \pm 1}$ were those calculated by Goldberg, Fadley, and Kono[28] and Manson and Cooper.[29] These inputs to the scattering calculation describe the amplitude and phase relationship between the photoelectron partial waves $l_i \pm 1$ as a function of the photoelectron kinetic energy. The atomic-scattering phase shifts were calculated using the atomic potentials tabulated by Moruzzi, Janak, and Williams.[30]

To account for vibration effects of the bulk atoms, the mean-square relative displacement (MSRD) was calculated using Eq. (33) of Ref. 4:

$$\langle u_i^2 \rangle \propto \frac{1}{M_i \theta_{D,i}} \left(1 + \frac{cT^2}{\theta_{D,i}^2} \cdots \right). \quad (5)$$

M_i is the atomic mass, $\theta_{D,i}$ is the correlated Debye temperature, T is the sample temperature, and c is a coefficient that varies slowly with temperature. For calculating the MSRD of

the bulk Ni (Cu) atoms, $\theta_{D,i}$ was 450 K (350 K) and T was 80 K. The effects of the surface atom vibrations on photoelectron diffraction data has been discussed previously.[12,31]

The surface sensitivity of ARPEFS in the study of clean surfaces is strongly dependent on the inelastic mean free path (IMFP). The IMFP calculation is important to high-precision modeling of such data. Certainly, many emitters lie several layers below the surface region and their signal never escapes the crystal. The IMFP was included using the exponential damping factor $e^{-r/\lambda}$, where λ was calculated using the Tanuma-Powell-Penn formula.[32]

Figure 2 plots the best fit (dashed line) overlaying the experimental ARPEFS data (solid line). For the MSSW calculation, a 74-atom cluster was used, the emission angle was optimized at $4°$ off normal, and the inner potential was optimized at 7.4 eV. The experimental Ni $3p$ ARPEFS amplitude was unusually low and was scaled by a factor of 5 to be consistent with the calculated amplitude. This scaling does not affect the results because the relative amplitudes and the oscillation frequencies were preserved. The spacing between the first two nickel layers was determined to be 2.09(3), which is a 3% expansion of the bulk value 2.03. A surface layer expansion is unexpected for the clean Ni(111) surface, but Hammer et al.[33] reported an expansion for the hydrogen-covered surface. Their low-energy electron diffraction (LEED) study of (2×2)-$2H$/Ni(111) determined that the top Ni layer is buckled and expanded an average of 1.5%. Thus, we expect that a significant amount of hydrogen was adsorbed during the angle-resolved photoemission spectroscopy data acquisition. Additionally, a surface buckling may explain the unusually low experimental oscillation amplitude because the surface layer would effectively become slightly disordered.

Figure 5(a) overlays the experimental Cu $3s$ ARPEFS data (solid line) with its best fit (dashed line). Figure 5(b) overlays the experimental Cu $3p$ ARPEFS data (solid line) with its best fit (dashed line). For each fit, a 74-atom cluster was used. The emission direction was found to be $5°$ off normal. Due to its unusually strong affect on the fit quality, the inner potential was fixed at 10 eV, as discussed above. The modeling calculations determined that $d_{1,2} = 2.06(5)$ Å, as compared to the bulk value of 2.09 Å. Previous LEED studies found a contraction of 0.7(5)%.[34,35]

VI. ERROR ANALYSIS

The best fit is determined by an R-factor minimization.[27,36] The parameters with the largest effect on the R factor were the spacing between the first two crystal layers and the photoemission angle. Figure 6 plots the R factor for the Ni $3p$ fitting as the Ni_1-Ni_2 interlayer spacing is varied.

The R factor as a function of the emission angle as measured from the surface normal θ_e and the azimuthal angle about the surface normal ϕ_e was minimized for both Cu data sets. These contour plots are illustrated in Figs. 7(a) and 7(b) for the Cu $3s$ and Cu $3p$ fitting calculations, respectively. The sample's orientation with respect to the photon beam, and thus the photon polarization vector, was maintained con-
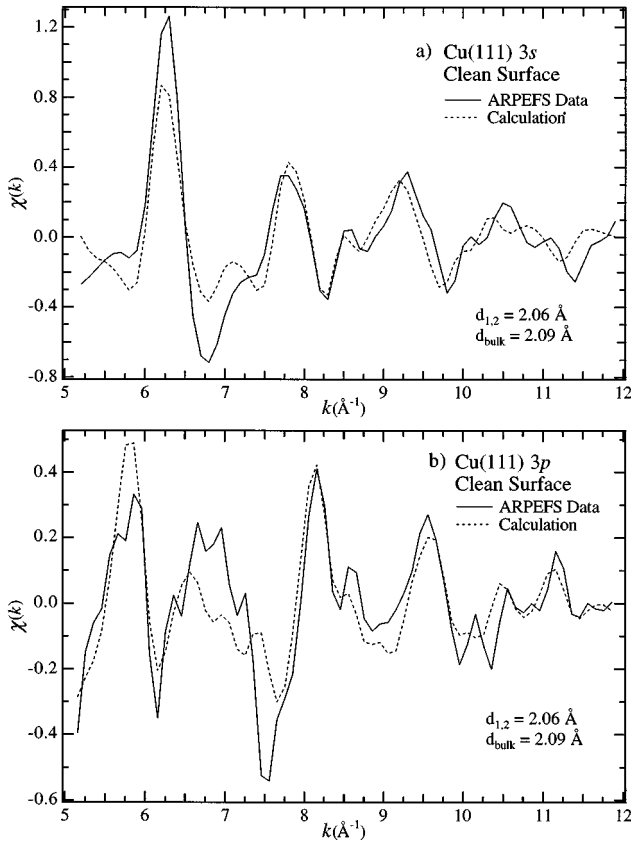
FIG. 5. ARPEFS $\chi(k)$ data (solid line) and the MSSW best fit (dashed line) for (a) Cu(111) $3s$ and (b) Cu(111) $3p$.

stant. θ_e was varied from $0°$ to $+10°$ stepping by $1°$ and ϕ_e was varied from $0°$ to $180°$ stepping by $10°$. The fcc surface is sixfold symmetric, but the bulk is threefold symmetric. The surface atoms are in the fcc threefold hollow site and $\phi_e = 0°$ was chosen to bisect one edge of the equilateral triangle formed by this threefold hollow site, the [100] direction. Thus a mirror plane exists and these R-factor calculations were symmetrized to obtain the results for $\phi_e = 180° - 360°$.
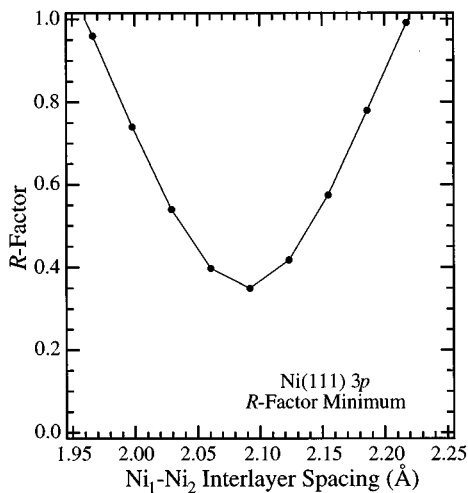
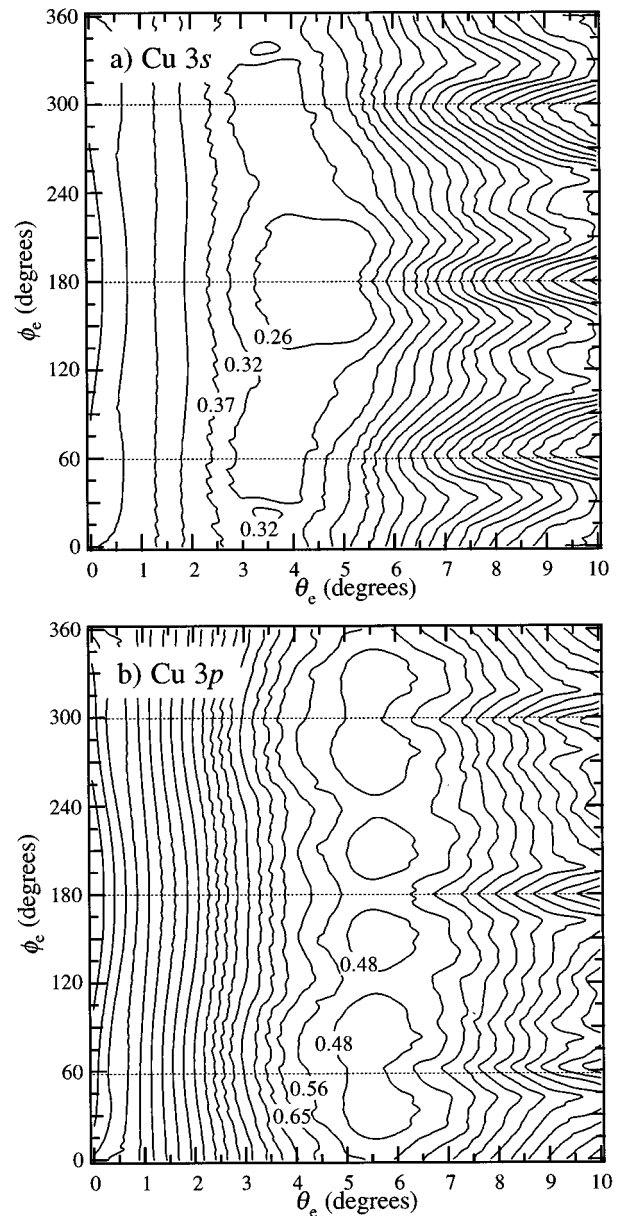FIG. 6. Ni $3p$ R-factor variation with the Ni_1-Ni_2 interlayer spacing.

FIG. 7. (a) Contour plot showing how the R factor varies with ϕ_e and θ_e for (a) the Cu $3s$ and (b) the Cu $3p$ modeling.

Comparing Figs. 7(a) and 7(b) shows some very interesting differences between the Cu $3s$ and the Cu $3p$ ARPEFS data. From Fig. 7(a) (the Cu $3s$ contour plot), the R-factor minimum is at $\theta_e = 4.5° \pm 1°$. The minimum is very shallow toward normal emission ($\theta_e = 0°$), but becomes steep more off normal ($\theta_e > 5°$). Figure 7(b) (the Cu $3p$ contour plot) is markedly different due to final-state effects. The R-factor minimum is $\theta_e = 5.5° \pm 0.5°$ is very steep both toward and away from normal emission ($\theta_e < 5°$, $\theta_e > 6°$). For the Cu $3p$ data, the $\theta_e = 0°$ fit was very poor, while the $\theta_e = 5°$ fit was quite good. These results have significant implications with respect to modeling ARPEFS data from non-s initial states.

The R factor also changes as a function of ϕ_e due to final-state effects. For both the $3s$ and the $3p$ initial states, the R factor is not sensitive to changing θ_e if θ_e is near normal emission ($\theta_e < 5°$). Even at the minimum (θe
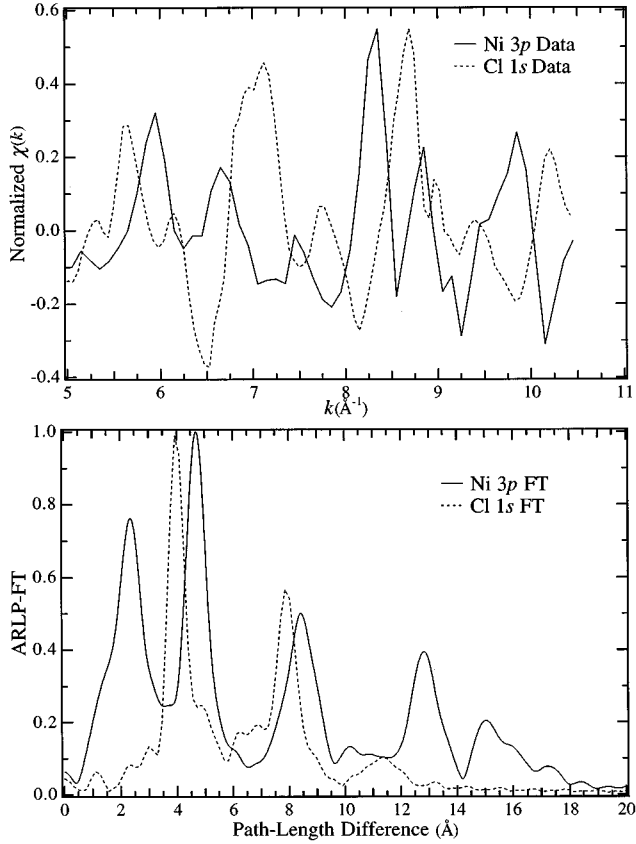
FIG. 8. The top panel overlayers the $(\sqrt{3} \times \sqrt{3})R30°$ Cl/Ni(111) (dashed line) with the Ni $3p$ (solid line) experimental ARPEFS curves. The bottom panel overlays their respective ARLP-based FT's.
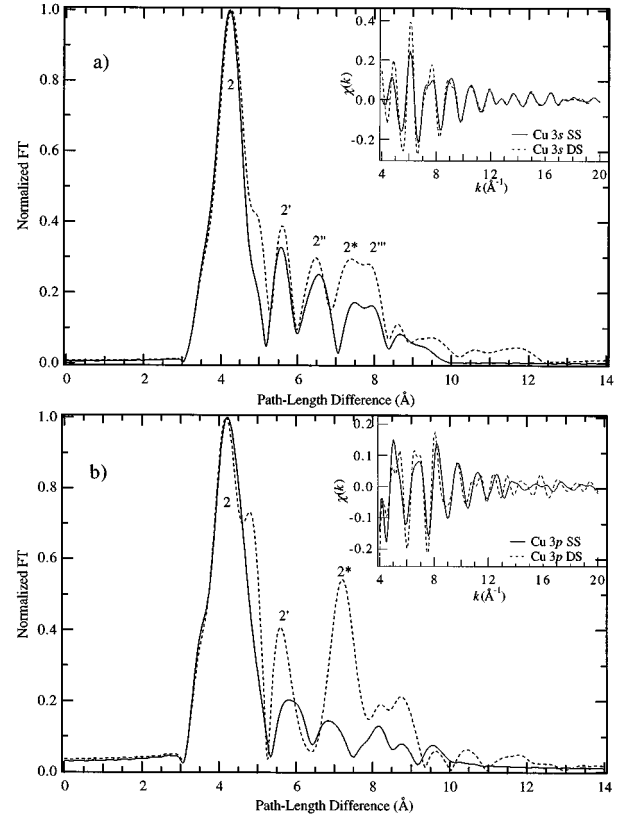

FIG. 9. FT of the calculated ARPEFS $\chi(k)$ curves (insets) for (a) Cu $3s$ and (b) Cu $3p$ where a single emitter was adsorbed 2.06 Å above a layer of scattering potentials for single scattering (solid line) and double scattering (dashed line).

VII. DISCUSSION

Figure 8 compares the Ni $3p$ data with $(\sqrt{3} \times \sqrt{3})R30°$Cl/Ni(111) data published previously.[37] This comparison illustrates the similarities and differences between adsorbate systems and clean surfaces as well as between s and p core-level initial-state ARPEFS data. As expected, the Cl $1s$ data and the Ni $3p$ data are roughly 180° out of phase.

Also, the FT's are remarkably similar, with ARLP-FT peaks for backscattering from layers below the source atom being resolved in both cases. The FT shows the slight lattice spacing difference between the two surfaces. Additionally, the Ni $3p$ FT's show a peak at ~ 2.5 Å due to effects described in Sec. IV, whereas the Cl $1s$ FT has no such peak.

Using the best-fit parameters for the Cu(111) $3s$ and $3p$ data, some test calculations were completed to study the scattering in more detail. The test cluster was a single emitter positioned 2.06 Å above a layer of scattering atomic potentials. The distance and geometry were chosen such that the layer simulated the second layer of the fcc Cu(111). In addition to testing for double scattering, this test allows for the simulation of the intensity differences between the Cu $3s$ and Cu $3p$ FT's in Fig. 4(b). Note that the ARLP method was not applied to these test $\chi(k)$ curves because they were calculated directly over a wide k range $(4-20 \text{ Å}^{-1})$.

This geometry should give rise to peaks at PLD's correlating with the 2 and 2′ positions for single scattering and the 2, 2′, and 2* positions for double scattering. Figure 9(a)
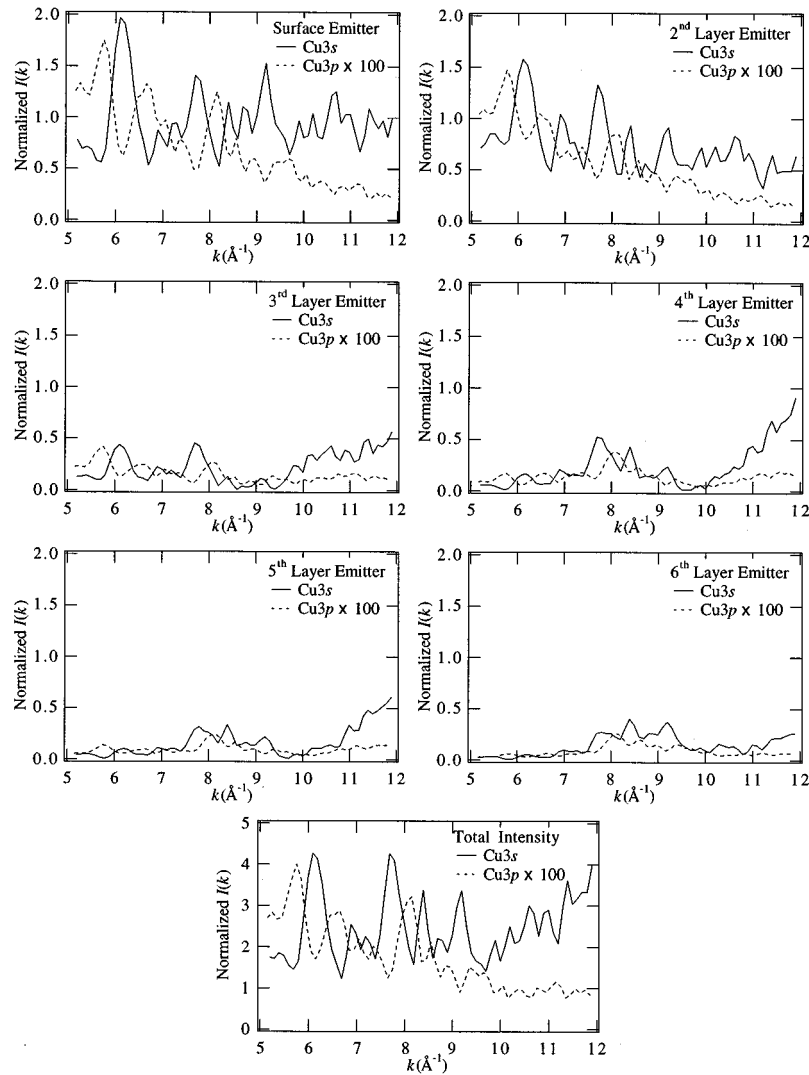
$\approx 5°$), the R factor remains rather insensitive to changing ϕ_e. However, for the $3p$ initial state, the threefold symmetry of the adsorption site begins to become evident. As θ_e is increased even more $(\theta_e > 5°)$, the R factor varies significantly with changing ϕ_e and the threefold symmetry of the adsorption site is evident in both contour plots. This effect is due to backscattering. As the emission angle becomes more off normal, backscattering from the second-layer Cu atoms is enhanced in the ARPEFS $\chi(k)$ curve.

These results from θ_e and ϕ_e indicate that the detected intensity distribution of Cu $3s$ photoemission is less directional than the detected intensity distribution of Cu $3p$ photoemission. As discussed previously, photoemission data from atomic s core-level initial states gives a p_0-wave final state. Thus the intensity distribution from the Cu $3p$ core-level initial states must have mostly d-wave character.

It should be noted that the calculations can be symmetrized as described above because the photon polarization vector is normal to the surface. Experience with fitting ARPEFS data suggests that the oscillation frequencies of the $\chi(k)$ curve are rather insensitive to the photon polarization vector orientation. However, the relative oscillation amplitudes are dependent on this orientation. These amplitude variations will change the magnitude of the R factor and perhaps break this threefold symmetry. Thus, if the photon polarization vector is significantly off normal, then ϕ_e should be calculated from 0° to 360°.

FIG. 10. Calculated ARPEFS $I(k)$ curves for Cu $3s$ (solid line) and Cu $3p$ (dashed line) where a single emitter was moved successively to deeper layers.

plots the Cu $3s$ FT for a single-scattering calculation (solid line) and a double-scattering calculation (dashed line). Figure 9(b) plots the Cu $3p$ FT for a single-scattering calculation (solid line) and a double-scattering calculation (dashed line). The insets show the respective $\chi(k)$ curves, which were filtered to pass only those PLD's greater than 3.5 Å, which removes some low-frequency oscillations unrelated to PLD's. The $2*$ peak distinctly appears in the Cu $3p$ FT even though there are only minor differences in the $\chi(k)$ curves. The $2*$ peak is not as convincing in the Cu $3s$ FT.

A striking difference between the Cu $3s$ and Cu $3p$ FT's is the occurrence of peaks $2''$ and $2'''$ in only the Cu $3s$ FT. Each additional prime represents scattering from the next laterally distant atomic potential. This difference is also observed in the ARLP-FT of the ARPEFS data for the peak $\lesssim 7$ Å and is the reason for the chosen $2*$ position in Fig. 4(b). These results again indicate that Cu $3p$ photoemission intensity is more directional than the Cu $3s$ photoemission intensity.

For the study of clean surfaces or multilayers, it is important to understand the contribution of emitters in subsurface layers to the overall $\chi(k)$ data. This test used a ten-layer fcc Cu(111) cluster with a single emitter. This emitter was subsequently moved from the surface to each layer, ending with the sixth. The cluster was constructed such that the photoemitted wave from the emitter in the sixth layer was subject to the same backscattering environment as the photoemitted wave from the emitter in the surface layer. This is true to four layers below the emitter, which is the cutoff seen in the ARLP FT of the ARPEFS data.

Figure 10 shows the multiple-scattering calculation results for this test cluster. The calculation parameters were fixed at the best-fit values discussed previously. The normalized intensity at the detector is plotted as a function of the magnitude of the photoelectron wave vector. The first point to note about these results is that the signal from the Cu $3s$ initial state is a factor of 100 stronger than the signal from the Cu $3p$ initial state. This factor drops out in Eq. (2) and is thus not seen in the data $\chi(k)$ curves. The reasons for this intensity difference are currently being studied. The next point to note is that the signal drops off drastically between placing the emitter in the second layer and placing the emitter in the

third layer. The signal increases slightly when placing the emitter in the fourth layer due to forward focusing by the surface layer atoms.

When the emitter is placed from the third layer to the sixth layer, the high-frequency oscillations important to ARPEFS become small and the $I(k)$ curves become dominated by the low-frequency oscillations (short path-length differences). This indicates that the signal becomes dominated by forward scattering.

The bottom panel in Fig. 10 plots $I_{total}(k)$, which is the sum of the six calculated $I(k)$ curves. This curve simulates the total intensity that would be collected. The low-frequency oscillations are removed by Eq. (3) when $I(k)$ is divided by a simple spline function to fit $I_0(k)$. The forward-scattering signal is therefore removed during the data reduction along with the standard $I_0(k)$. The resulting experimental ARPEFS $\chi(k)$ curve is thus dominated by backscattering. Although the signal from the deeper layers may modulate the high-frequency oscillation magnitudes slightly, the signal is principally due to photoemission from the first two crystal layers. Scattering from six or seven layers is therefore adequate to simulate ARPEFS data.

VIII. CONCLUSION

To better understand the ARPEFS technique, we studied s and non-s initial-state photoemission from clean metal surfaces. As expected, the Cu $3s$ $\chi(k)$ curve is roughly 180° out of phase from the Cu $3p$ $\chi(k)$ curve. The clean surface ARPEFS data resemble data for adsorbate systems, showing strong backscattering signals from atoms up to four layers below the source atoms. In addition to the backscattering, the Ni $3p$ data and Cu $3p$ data show a peak in the FT at ~ 2.5 Å corresponding to in-plane single scattering of the photoemission wave.

Although there were many layers of emitters in this clean surface study, the ARPEFS fitting process was sensitive to the surface relaxation. The spacing between the first two nickel layers is 2.09(3) Å, which is a 3% expansion from the bulk nickel value. This result indicates that hydrogen was adsorbed on the surface during the data acquisition. By contrast, the spacing between the first two copper layers is 2.06(5) Å.

For the Cu(111) $3s$ and $3p$ fitting, the R factor was minimized as a function of ϕ_e and θ_e. These contour plots illustrate that the Cu $3p$ photoemission intensity is more directional than the Cu $3s$ photoemission intensity. This in turn indicates that the photoemission intensity from the Cu $3p$ core levels must have mostly d wave character.

To study the scattering processes in more detail, two types of test calculations were completed. A cluster with a single emitter adsorbed on a layer of scattering potentials was used to investigate the possibility of detecting double-scattering events directly in the FT. To this end, the Cu $3p$ test results were more convincing than the Cu $3s$ test results. A second test system used a ten-layer cluster and a single emitter moved successively through the first six layers. Although the signal from the deeper layers may modulate the high-frequency oscillation magnitudes slightly, the photoemission signal comes principally from the first two crystal layers.

It has been shown that photoelectron holography signals from clean surfaces are dominated by forward scattering, with atomic positions being imaged up to three layers *ahead* of the emitting atom.[38] A combination of these two photo-electron diffraction techniques would therefore provide a very good method for studying ordered interfaces.

[1] S. D. Kevan, D. H. Rosenblatt, D. Denley, B. C. Lu, and D. A. Shirley, Phys. Rev. Lett. **41**, 1565 (1978).

[2] J. J. Barton, C. C. Bahr, Z. Hussain, S. W. Robey, J. G. Tobin, L. E. Klebanoff, and D. A. Shirley, Phys. Rev. Lett. **51**, 272 (1983).

[3] D. P. Woodruff, D. Norman, B. W. Holland, N. V. Smith, H. H. Farrell, and M. M. Traum, Phys. Rev. Lett. **41**, 1130 (1978).

[4] M. Sagurton, E. L. Bullock, and C. S. Fadley, Surf. Sci. **182**, 287 (1987).

[5] Y. Zheng and D. A. Shirley, Chem. Phys. Lett. **203**, 114 (1993).

[6] J. J. Barton, C. C. Bahr, S. W. Robey, Z. Hussain, E. Umbach, and D. A. Shirley, Phys. Rev. B **34**, 3807 (1986).

[7] S. W. Robey, C. C. Bahr, Z. Hussain, J. J. Barton, K. T. Leung, J. R. Lou, A. E. S. v. Wittenau, and D. A. Shirley, Phys. Rev. B **35**, 5657 (1987).

[8] L. Q. Wang, A. E. S. v. Wittenau, Z. G. Ji, L. S. Wang, Z. Q. Huang, and D. A. Shirley, Phys. Rev. B **44**, 1292 (1991).

[9] Z. Q. Huang, L. Q. Wang, A. E. S. v. Wittenau, Z. Hussain, and D. A. Shirley, Phys. Rev. B **47**, 13 626 (1993).

[10] Z. Q. Huang, Z. Hussain, W. T. Huff, E. J. Moler, and D. A. Shirley, Phys. Rev. B **48**, 1696 (1993).

[11] Y. Zheng, E. Moler, E. Hudson, Z. Hussain, and D. A. Shirley, Phys. Rev. B **48**, 4960 (1993).

[12] W. R. A. Huff, Y. Chen, X. S. Zhang, L. J. Terminello, F. M. Tao, Y. K. Pan, S. A. Kellar, E. J. Moler, Z. Hussain, H. Wu, Y. Zheng, X. Zhou, A. E. S. v. Wittenau, S. Kim, Z. Q. Huang, Z. Z. Yang, and D. A. Shirley, Phys. Rev. B **55**, 10 830 (1997).

[13] W. R. A. Huff, Y. Zheng, Z. Hussain, and D. A. Shirley, J. Phys. Chem. **98**, 9182 (1994).

[14] J. C. Tang, Chin. Phys. Lett. **4**, 321 (1987).

[15] S. Y. Tong and J. C. Tang, Phys. Rev. B **25**, 6526 (1982).

[16] M. Biagini, Phys. Rev. B **48**, 2974 (1993).

[17] S. D. Kevan, Ph.D. thesis, University of California at Berkeley, 1980.

[18] Z. Hussain, W. R. A. Huff, S. A. Kellar, E. J. Moler, P. A. Heimann, W. McKinney, H. A. Padmore, C. S. Fadley, and D. A. Shirley J. Electron Spectrosc. Relat. Phenom. **80**, 401 (1996).

[19] J. J. Barton, S. W. Robey, and D. A. Shirley, Phys. Rev. B **34**, 778 (1986).

[20] J. J. Barton, Ph.D. thesis, University of California at Berkeley, 1985.

[21] J. J. Barton, Z. Hussain, and D. A. Shirley, Phys. Rev. B **35**, 933 (1987).

[22] L. J. Terminello (private communication).

[23] J. J. Barton and D. A. Shirley, Phys. Rev. B **32**, 1892 (1985).

[24] A. Kaduwela, Ph.D. thesis, University of Hawaii at Manoa, 1991.

[25] J. J. Rehr and R. C. Albers, Phys. Rev. B **41**, 8139 (1990).

[26] D. J. Friedman and C. S. Fadley, J. Electron Spectrosc. Relat. Phenom. **51**, 689 (1990).

[27] Y. Chen, H. Wu, and D. A. Shirley (unpublished).

[28] S. M. Goldberg, C. S. Fadley, and S. Kono, J. Electron Spectrosc. Relat. Phenom. **21**, 285 (1981).

[29] S. T. Manson and J. W. Cooper, Phys. Rev. **165**, 126 (1968).

[30] V. L. Moruzzi, J. F. Janak, and A. R. Williams, *Calculated Electronic Properties of Metals* (Pergamon, New York, 1978).

[31] R. E. Allen, G. P. Alldredge, and F. W. d. Wette, J. Chem. Phys. **54**, 2605 (1971).

[32] S. Tanuma, C. J. Powell, and D. R. Penn, Surf. Interface Anal. **20**, 77 (1993).

[33] L. Hammer, H. Landskron, W. Nichtl-Pecher, K. A. Fricke, Heinz, and K. Muller, Phys. Rev. B **47**, 15 969 (1993).

[34] S. P. Tear, K. Roll, and M. Prutton, J. Phys. C **14**, 3297 (1981).

[35] S. A. Lindgren, L. Wallden, J. Rundgren, and P. Westrin, Phys. Rev. B **29**, 576 (1984).

[36] W. H. Press, S. A. Teukolsky, W. T. Vetterling, and B. P. Flannery, *Numerical Recipes in Fortran: The Art of Scientific Computing* (Cambridge University Press, Cambridge, 1992).

[37] L.-Q. Wang, Z. Hussain, Z. Q. Huang, A. E. S. v. Wittenau, D. W. Lindle, and D. A. Shirley, Phys. Rev. B **44**, 13 711 (1991).

[38] B. L. Petersen, L. J. Terminello, J. J. Barton, and D. A. Shirley, Chem. Phys. Lett. **213**, 412 (1993).